

Article

# Comparing Landsat and RADARSAT for Current and Historical Dynamic Flood Mapping

Ian Olthof \* and Simon Tolszczuk-Leclerc

Canada Centre for Mapping and Earth Observation, Natural Resources Canada, 560 Rochester St, Ottawa, ON K1S 5K2, Canada; simon.tolszczuk-leclerc@canada.ca

\* Correspondence: ian.olthof@canada.ca; Tel.: +1-613-759-6275

Received: 3 April 2018; Accepted: 17 May 2018; Published: 18 May 2018



**Abstract:** Mapping the historical occurrence of flood water in time and space provides information that can be used to help mitigate damage from future flood events. In Canada, flood mapping has been performed mainly from RADARSAT imagery in near real-time to enhance situational awareness during an emergency, and more recently from Landsat to examine historical surface water dynamics from the mid-1980s to present. Here, we seek to integrate the two data sources for both operational and historical flood mapping. A main challenge of a multi-sensor approach is ensuring consistency between surface water mapped from sensors that fundamentally interact with the target differently, particularly in areas of flooded vegetation. In addition, automation of workflows that previously relied on manual interpretation is increasingly needed due to large data volumes contained within satellite image archives. Despite differences between data received from both sensors, common approaches to surface water and flooded vegetation mapping including multi-channel classification and region growing can be applied with sensor-specific adaptations for each. Historical open water maps from 202 Landsat scenes spanning the years 1985–2016 generated previously were enhanced to improve flooded vegetation mapping along the Saint John River in New Brunswick, Canada. Open water and flooded vegetation maps were created over the same region from 181 RADARSAT 1 and 2 scenes acquired between 2003–2016. Comparisons of maps from different sensors and hydrometric data were performed to examine consistency and robustness of products derived from different sensors. Simulations reveal that the methodology used to map open water from dual-pol RADARSAT 2 is insensitive to up to about 20% training error. Landsat depicts open water inundation well, while flooded vegetation can be reliably mapped in leaf-off conditions. RADARSAT mapped approximately 8% less open water area than Landsat and 0.5% more flooded vegetation, while the combined area of open water and flooded vegetation agreed to within 0.2% between sensors. Derived historical products depicting inundation frequency and trends were also generated from each sensor's time-series of surface water maps and compared.

**Keywords:** RADARSAT; Landsat; surface water; time-series

## 1. Introduction

Water is both a vital resource and a hazard during flooding whose distribution simultaneously influences and is a result of land use and climate. Mapping the location of water and how frequently it is present is critical to all water-related issues. At the ends of the location-frequency spectrum are permanently inundated water bodies and permanently dry land that is never inundated. Between these two extremes are areas where surface water is ephemeral. The timing of ephemeral water is often seasonal as in the case of springtime flooding due to snowmelt at high latitudes or monsoon in the tropics, while its occurrence is becoming more difficult to predict due to increasingly frequent extreme weather events [1]. Although many regions in Canada flood annually during the spring melt

season including the Saint John River Basin in New Brunswick, in recent years severe and unexpected flooding has occurred in major cities including Calgary and Toronto in late-spring and summer of 2013, and Ottawa and Montreal in the spring of 2017, all caused primarily by record rainfall events. Floodplain characterization that provides knowledge of the location and frequency of flooding caused by both seasonal and extreme weather events is critical for public safety, as well as land use planning, land valuation and insurance.

Geospatial products mapping surface water and its dynamics have been generated at regional [2,3], continental [4] and global scales [5–8]. While all of these products have been created using medium resolution optical imagery from the Landsat archive due to its long record and data availability, operational flood mapping in Canada relies mainly on imagery from Canada's RADARSAT-2 satellite with plans to migrate to the RADARSAT Constellation Mission (RCM) once launched in 2018. Member countries of the International Charter on Space and Major Disasters including Canada also use ALOS, ENVISAT, Sentinel-1 and TerraSAR-X among other radar satellites as primary data sources for flood mapping.

Radar is a preferred sensor for operational flood mapping because it is able to penetrate cloud cover that often persists during flood events, and it has the added benefit of performing well for surface water mapping [9]. Its ability to penetrate cloud increases the likelihood of imaging peak flood conditions that are critical to map the full extent of historical inundation. However, the RADARSAT image archive does not extend as far back in time as Landsat, and a lack of standard coverage due to satellite tasking has rendered the record sparse in some regions. Nonetheless, combining optical and radar for both operational and historical surface water mapping provides timelier flood information, and a more complete range of historical surface water extents than either sensor on its own. Generating consistent information from multiple sensors is challenging however, especially between those that fundamentally interact with the target differently as in the case of optical and radar.

During severe events, flooding often occurs beneath vegetation and in the case of several of the worst events in Canada in recent years, extensively in developed areas. Mapping flooded vegetation from optical sensors is mature and has known limitations [10], while research to map flooded vegetation from radar has been active in recent years [11,12]. Detecting water beneath vegetation in optical imagery is challenging during the growing season because the canopy obscures the water surface [13–15], however sufficient absorption generally occurs to detect water during leaf-off in early spring or late fall in wavelengths from visible to infrared. Landsat's look direction within  $\pm 7.5^\circ$  of nadir [16] enhances its ability to sense water in leaf-off conditions due to the predominantly vertical structure of vegetation, while radar is able to detect water at an oblique angle beneath leaf-on canopies under certain conditions, depending on leaf size, shape and orientation, as well as wavelength, polarization and incidence angle. Longer wavelengths relative to leaf size [14] and shallower incidence angles [17] generally provide greater signal penetration through the canopy. Once the incident radar signal has penetrated the canopy, double-bounce scattering [18] off the water surface and vertical stems and trunks acting as corner reflectors generates a high intensity return to the sensor [19]. Backscatter generally decreases with increasing incidence angle for different forest types; however, separation between flooded and non-flooded forest remains relatively constant with incidence angle [20].

To date, open water that is usually dark in radar due to specular reflection has been mapped using single polarization thresholding, even when multiple polarizations are available [21,22]. While thresholding has been shown to perform well for open water under ideal conditions, water surface roughness is mainly caused by wind and waves as well as wet ice [23,24] that is sometimes present during the spring flood season. These conditions can produce diffuse reflection that increases backscatter to a level where a single threshold value cannot reliably separate water from land [25]. Automated methods used to determine optimal threshold values are compromised by these factors, while manual thresholding can be better tuned to minimize errors of omission and commission. Even still, a significant amount of post-processing is often required to reduce errors to an acceptable

level [26]. The current application of generating dynamic surface water information from Earth Observation data requires a time-series of surface water maps as input, each of which needs to be classified independently. While manual supervised methods including thresholding exist to reliably extract surface water information from both optical and radar data, automated methods are preferred due to the number of scenes required to generate a dynamic map representative of historical surface water conditions.

Information contained in multiple radar polarizations can help reduce errors in open water extraction, though making use of this information requires a classification approach other than single channel image thresholding. Supervised multispectral classification has long been used in terrestrial remote sensing applications [27], but has been under-utilized for surface water extraction from radar. One challenge is that supervised classification approaches require spectral signatures for each class to train the classifier; in the case of water extraction, signatures representing land and water. Classifying land and water with standard spectra will not achieve an optimal classification result for several reasons. First, the spectral variability of water in radar due to wind and ice leads to confusion between water and land. Second, the spectra of land also varies due to the presence of several land cover types that change in time because of vegetation phenology, moisture and atmosphere [28,29]. An additional complicating factor is that in order to perform a traditional supervised classification such as minimum distance or maximum likelihood, separate signatures must be obtained for all land cover types present in the scene. To deal with these limitations across hundreds of scenes, an automated open surface water extraction methodology that is an extension of one already developed in [3] is implemented in this paper. The approach makes use of recently available inundation frequency products from historical Landsat data [3,30] to sample scene-specific signatures representing land and water that are input into machine learning for classification.

Once open water has been mapped, flooded vegetation is detected next by exploiting the fact that it normally occurs adjacent to open water and has a high intensity return caused by double bounce in radar. Applying a single high threshold value to an entire scene to extract flooded vegetation generally produces high commission error, as other bright double bounce targets unrelated to flooding such as buildings are often falsely included as flooded vegetation. Therefore, as recommended by [31], the approach developed in this paper minimizes commission error by combining thresholding with region growing seeded in open water.

This paper presents integration between optical and radar sensor data for mapping historical surface water dynamics. A similar approach was used to extract consistent information from both sensor types that uses machine learning for open water and region growing for flooded vegetation. We automated the classification of 181 historical RADARSAT 1 and 2 images from 2003–2016 into land, open water and flooded vegetation, and stacked them to generate dynamic surface water maps representing historical inundation frequency and trends. Maps generated from 202 Landsat scenes from 1985–2016 used to create inundation frequency products in [3] were enhanced to better represent flooded vegetation in leaf-off conditions and stacked to generate the same dynamic surface water products as radar. Comparisons of coincident maps were performed for both open water and flooded vegetation as well as with hydrometric water gauge levels. Finally, dynamic surface water products were compared against each other, and against global water occurrence mapped in [30].

## 2. Materials and Methods

### 2.1. Data

#### 2.1.1. Study Area

The Saint John River flows from Maine to the Bay of Fundy and forms the Canada-US border along parts of its length (Figure 1). Most of the river's 673 km length is located in the province of New Brunswick, and is nearly 3 km across at its widest point just north of the City of Saint John near the Bay of Fundy. Annual springtime flooding occurs along much of its length, but is most severe along

a 55 km stretch from Fredericton to Gagetown where ice jams form in an area of expansive floodplains with low relief. Hydrometric flood gauge data from Environment Canada show that maximum water depth was generally reached between mid-April to early May from 1985 to 2016 at the Maugerville station. A study mask covering a 3065 km<sup>2</sup> area including the main river system and floodplains from Fredericton to Saint John was used to extract open water and flooded vegetation extents for comparison between sensors and hydrometric water depth data described below.

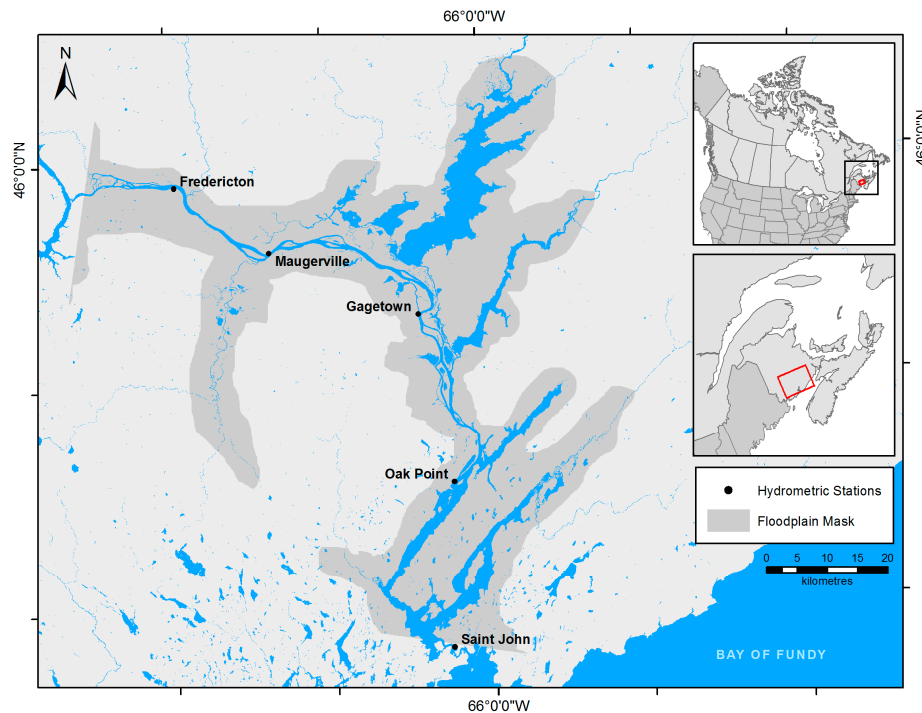


**Figure 1.** Study area along the Saint John River including the floodplain mask and hydrometric stations at Maugerville and Oak Point.

### 2.1.2. Landsat

The same Landsat open water products presented in [3] were used in the current analysis. Scenes are 30 m resolution from path 10, row 28 covering the Saint John River Basin including Fredericton and Saint John at the mouth to the Bay of Fundy. A total of 202 scenes from 1985–2016 from Landsat 5 TM, Landsat 7 ETM+ and Landsat 8 OLI acquired in the spring and summer between the months of March and August were downloaded from the USGS Earth Explorer archive. Images were selected to include only those with a minimum 40% clear-sky area within the scene. Each scene was cloud screened using FMask [32], calibrated to Top-of-Atmosphere reflectance [33], and then classified to open water and land using multispectral See5 decision tree [34] classification with 1:50 k National Hydrographic Network (NHN) water base data for training. Validation of summer 2002 open water Landsat maps was performed against orthophotos acquired during the same summer, generating over 97% overall classification accuracy. Water extents from individual maps were also significantly related to coincident hydrometric water depth at  $p < 0.001$  [3].

### 2.1.3. RADARSAT

RADARSAT 1 is a Canadian C-band synthetic aperture radar (SAR) satellite that operated between 1995 and 2013 acquiring data in single HH polarization. RADARSAT 2 is the follow-on mission that was launched in 2007, representing a significant improvement over RADARSAT 1 by providing the ability to acquire data in four polarizations (quad-pol:HH, HV, VH, VV:HH, HV, VH, VV where H

is horizontal polarization and V is vertical polarization; the first polarization is transmitted and the second received).

A total of 72 RADARSAT 1 scenes were ordered over the same region as Landsat path 10/row 28 between 2003 and 2012 from the RADARSAT archive through the Canadian Space Agency. Scenes were delivered as SAR Georeferenced Fine Resolution (SGF) products at 12.5 m resolution. Anniversary dates were as early as 5 March, with a median anniversary date of 5 May for all 72 scenes. Upon inspection of the data after initial processing, it was noted that most RADARSAT 1 scenes were acquired too early in the spring, causing significant overlap between land and water in single-pol intensity due to diffuse reflection caused by wind and/or ice. Therefore, a set of 21 scenes with an earliest date of 4 May and a median anniversary date of 5 June was selected based on visual assessment of initial water classifications.

An additional 162 12.5 m resolution RADARSAT 2 scenes were downloaded through the National Earth Observation Data Framework (NEODF-[https://neodf.nrcan.gc.ca/neodf\\_cat3/](https://neodf.nrcan.gc.ca/neodf_cat3/)) catalog, four of which were single HH polarization, while the remaining 158 were either HH/HV or VV/VH dual-polarization. Of these 162 scenes, only two were deemed unsuitable to include in the stack analysis based on high omission or commission error determined from a visual inspection of initial results, one of which was single-polarization. The earliest anniversary date for the remaining 160 RADARSAT 2 scenes was 9 April, with a median anniversary date on 29 June, which is one week later than the median date for Landsat on 22 June (Table 1). In some cases, two to three RADARSAT 2 scenes were acquired on the same day, producing 131 dates of imagery from all 181 RADARSAT 1 and 2 scenes. All images were either path (SGF) or path image plus (SGX) products acquired in either standard or wide mode. Near range incidence angles varied between 19.2 and 48.7 degrees, while far angles ranged from 27.2 to 52.2 degrees.

**Table 1.** Satellite data dates and coincident water depth by sensor.

Satellite/Sensor	Scenes	Resolution	Earliest	Median	Year Range	Mean Water Depth	Max Water Depth
RADARSAT 1	21	12.5 m	4-May	5-June	2003–2012	2.90 m	6.50 m
RADARSAT 2	160	12.5 m	9-April	29-June	2008–2016	2.96 m (2008–2015)	7.09 m (2008–2015)
Landsat 5	95	30 m	27-March	16-June	1985–2011		6.73 m
Landsat 7	82	30 m	11-March	28-June	1999–2016	2.50 m (1985–2015)	(1985–2015)
Landsat 8	25	30 m	10-April	7-July	2013–2016		

#### 2.1.4. Hydrometric Data

Daily hydrometric water level data were acquired through Environment Canada’s National Hydrological Service web portal for Maugerville and Oak Point monitoring stations from 1985–2015. These stations were selected because they are located upstream and downstream of the major floodplain on the Saint John River, while providing a near continuous water level record for the 1985–2015 period.

#### 2.1.5. High-Resolution Imagery

High-resolution images were sought to verify open water and flooded vegetation extraction from Landsat and RADARSAT. Fifteen high-resolution scenes of the Saint John region were available through the National Earth Observation Data Framework Catalogue (NEODF-[https://neodf.nrcan.gc.ca/neodf\\_cat3/](https://neodf.nrcan.gc.ca/neodf_cat3/)), however none were acquired on the same date as any Landsat or RADARSAT scenes. Hydrometric water depth was determined on acquisition dates for each Landsat, RADARSAT and available high-resolution scene. Based on water depth and location, a single QuickBird scene acquired on 25 April during the 2009 spring flood was found to have a similar water depth (6.706 m) to a Landsat 5 and RADARSAT 2 scene both acquired on the same day during the 2008 spring flood (6 May 2008–6.725 m water depth). While similar water depth does not guarantee similar flood extent due to water movement, we assume that at a broad level and for visual comparison, a general

depth-extent relation exists between dates. This QuickBird scene was available in natural color at 0.6 m resolution and included areas of flooded vegetation along a ~12 km stretch of the Saint John River from Fredericton to Maugerville. Visual comparisons between QuickBird and classified Landsat and RADARSAT open water and flooded vegetation were conducted to verify extraction methods.

## 2.2. Flood Mapping

### 2.2.1. Landsat

Landsat open water classifications produced in [3] were enhanced by region growing from open water dark areas that generally represented flooded vegetation. Although no field data was available to determine whether vegetation was flooded, the known spectral response of flooded vegetation in Landsat and RADARSAT as well as high-resolution imagery in Google Earth showing shrub and treed areas on the floodplain and other imagery from NEODF representing both flooded and non-flooded states were visually interpreted to confirm flooded vegetation. Region growing in Landsat was performed by evaluating and classifying adjacent pixels as flooded vegetation that simultaneously satisfied the criteria of reflecting less than 1.5% in red, less than 1% in NIR and less than 0.2% in SWIR 1 in units of percent TOA reflectance. Region growing began in open water and continued iteratively to classify flooded vegetation pixels to a maximum of 200 iterations or until adjacent pixels no longer satisfied the dark threshold criteria.

### 2.2.2. RADARSAT

Machine learning such as Random Forest and See5 Decision Trees, Neural Networks and Support Vector Machines have become increasingly popular to address remote sensing classification problems in recent years [35]. These have advantages over more traditional classifiers such as maximum likelihood largely because they are non-parametric and therefore perform well regardless of spectral class distributions. This is especially advantageous when automating classifications without user input, since class signatures do not need to be checked to see if they violate statistical assumptions.

Open water was classified in individual RADARSAT scenes using See5 decision trees and scene-specific training data representing water and land. Permanent land and water masks were produced from combined spring and summer 1985–2016 Landsat inundation frequency products published in [3], where permanent water was assigned to water bodies that were permanently inundated (100% inundation frequency) and permanent land where frequency was 0%. Training was done using the See5 default parameters of 10 trials, a confidence factor of 0.25 and no winnowing. In single-polarization imagery that included all 21 RADARSAT 1 images and three HH polarization RADARSAT 2 images, See5 produced a simple intensity threshold model. Final open water classifications were improved by first reassigning roads that are single-bounce targets often mistakenly classified as water to land using a 2010 30 m Landsat land cover of Canada [36], and then sieved to exclude objects smaller than 50 pixels (~0.8 ha).

Flooded vegetation was subsequently region grown from open water using a single, sigma-naught calibrated polarization applied to enhance bright targets. Like-polarizations (HH or VV) were used to map flooded vegetation since they generally provided better contrast between flooded vegetation and other targets [37]. Region growing was performed twice; first to detect bright double-bounce targets above a specified intensity threshold value, and then a second time using a conservative dark threshold value to infill areas contained within bright flooded vegetation and better connect nearby areas of open water. Tests were conducted to determine optimal bright and dark threshold values. Based on these, it was determined that separate threshold values were required depending on incidence angle far range, with dark and bright thresholds set to 0.1 and 0.5 sigma-naught values for far range angles less than 35 degrees, and 0.21 and 0.025 for far range angles greater than 35 degrees. Region growing continued until no pixels met the bright threshold criterion to a maximum of 200 iterations, and then until no pixels met the dark threshold criterion or 100 iterations. Image speckle and diffuse scattering

caused by waves on water led to omission error that was minimized by sieving land objects that were smaller than islands and completely contained within open water or flooded vegetation. Finally, a DEM from the Canadian Digital Elevation Database (CDED) was used to remove false detections occurring on slopes greater than 3.5 degrees (Figure 2).

## Flood Mapping Workflow

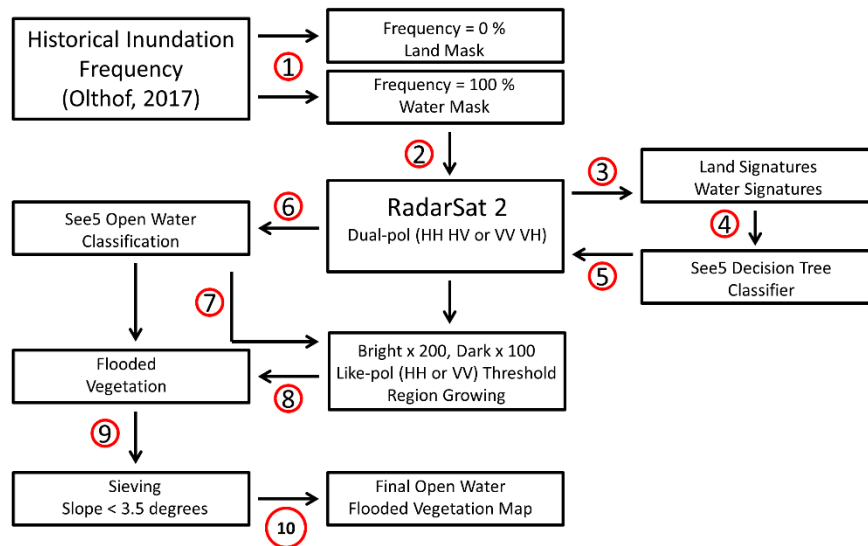


Figure 2. RADARSAT 2 open water and flooded vegetation mapping methodology.

Quality control through visual assessment was important to correct problems and ensure that surface water products included in the stack analyses were of high quality. Validation of individual water maps is difficult due to a lack of synchronous reference data. Images of each individual classification were created in a bitmap file format to enable efficient quality control by providing the ability to quickly identify and remove scenes that had significant omission or commission error.

### 2.3. Sensitivity of RADARSAT 2 Open Water Mapping to Training Error

Inundation frequency maps used to generate permanent land and water masks may not be perfectly representative of flood conditions especially during extreme events, and may therefore introduce error in the training data where water pixels are falsely assigned to the land class (water omission) and vice-versa (water commission). Radar's ability to penetrate cloud cover produces a higher probability of imaging peak flood conditions, and therefore maximum inundation extent may be higher in radar than in optical. When classifying a radar image representing peak flood conditions, greater surface water area in radar compared to historical inundation based on Landsat will cause water omission errors in the training data. Decision tree classifiers are known to be highly robust to training error [38]; however, robustness depends on the classification problem including the number of classes. Therefore, simulations were conducted to explore the sensitivity of RADARSAT classification accuracy to labelling errors in training data.

A single RADARSAT 2 image was selected for this experiment that was acquired August 8, 2008 near mid-summer to coincide as closely as possible with 1:50 k (NHN) waterbodies representing normal water extents used as a reference to evaluate classification performance. Training labelling errors of water omission, water commission and random errors of both omission and commission were evaluated separately in two percent increments from zero to 60%. Omission errors were introduced in the training data by randomly assigning pixels sampled beneath the water mask to the land class,

while commission errors were introduced by doing the opposite of randomly assigning land pixels to water. Random errors were introduced by simultaneously introducing water omission and commission errors in the training data. For each type of error and at each error level, classification accuracy was evaluated using NHN water extents as truth. Cohen's kappa statistic that accounts for agreement due to random chance [39] was used as the measure of overall accuracy and plotted as a function of percent training error.

#### 2.4. Surface Water Dynamics

##### 2.4.1. Inundation Frequency

Whereas previously in [3], separate spring and summer seasonal Landsat inundation products were generated from annual composites, inundation was generated in this study using all images simultaneously from 1985–2016, and separately from 2003–2016 for direct comparison with inundation over the same period from RADARSAT. Inundation frequency was calculated per pixel as the percentage of valid observations that each pixel was flooded through time, and was produced for open water only and for open water and flooded vegetation combined. Inundation frequency objects were sieved to exclude those smaller than 6.75 km<sup>2</sup> with a frequency less than five percent, and those smaller than 0.9 km<sup>2</sup> with a frequency less than ten percent. Inundation frequency was calculated from the RADARSAT map stack in the same manner except at 12.5 m instead of 30 m resolution.

##### 2.4.2. Inundation Trends

The application of per-pixel linear regression to image time-series has been used extensively to map trends in continuous dependent variables such as NDVI [40,41], water fraction [42] and Leaf Area Index (LAI) [43], among other parameters. Logistic regression is appropriate to predict a binary response variable, and has been applied in the remote sensing literature to determine variable importance to categorical ratings including flood susceptibility [44] and landslide hazard [45]. To the authors' knowledge, logistic regression has not been applied to map frequency trends in binary categorical outcomes such as land versus water. Inundation trend maps were generated from separate Landsat and RADARSAT map time-series using per-pixel binomial logistic regression with number of days since the earliest scene date as the independent variable, and land/water from stacked water maps as the binary dependent variable. Output images include the regression coefficient indicating the direction of the trend towards water or land, and a chi-squared significance test *p*-value indicating the probability that the observed trend was real.

### 3. Results

#### 3.1. Training Error

For the three types of labelling error introduced into training data (water omission, commission and random), kappa was over 0.84 at 0% training error, indicating excellent agreement due to good classification performance and a RADARSAT image representative of baseline water extents mapped by NHN. When random errors were introduced into the training data, overall accuracy remained above 0.8 to 38% training error before suddenly dropping to 0% above 50% error due to the classification predicting water for all pixels in the image. Whether water omission or commission error was introduced into the training data, classification performance was similar with kappa remaining above 0.8 to 30–40% training error before dropping to 0 above 50% (Figure 3).

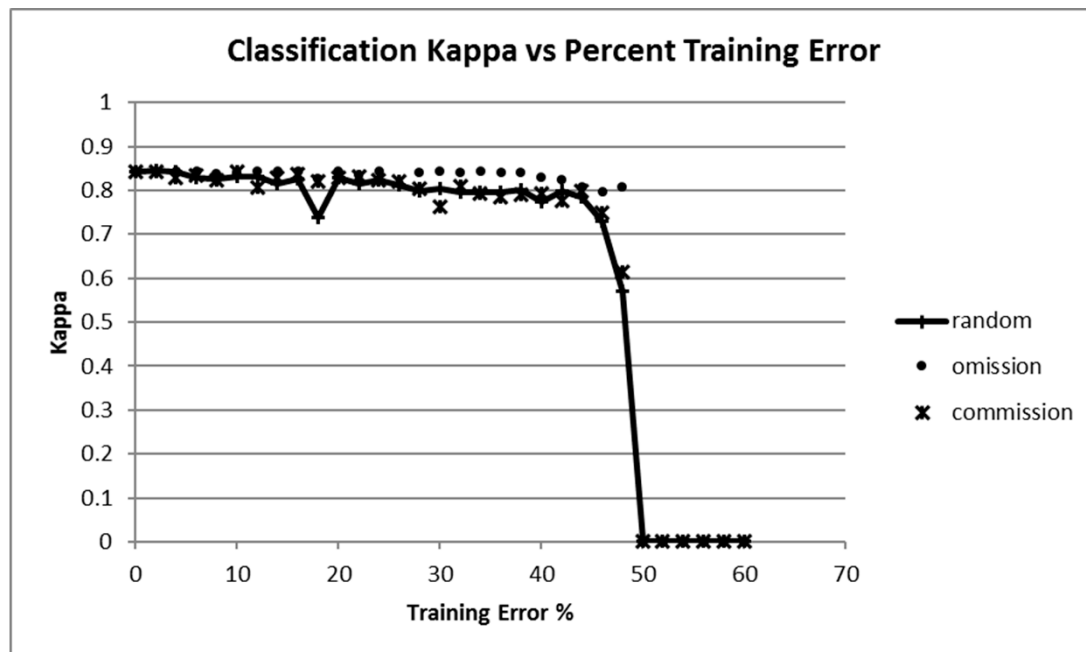


**Figure 3.** Classification accuracy measured by Cohen's kappa coefficient as a function of random, water omission and water commission training labelling error.

### 3.2. Comparison between RADARSAT 2 and Landsat Flood Extents

Open water and flooded vegetation extents were extracted from 11 RADARSAT 2 scenes acquired on the same dates as seven Landsat scenes, with multiple RADARSAT 2 images acquired on the same date as individual Landsat scenes in some cases. NHN water area and flood extents from Landsat and RADARSAT were extracted for comparison beneath a common area represented by RADARSAT 2 image footprints where corresponding Landsat imagery was cloud-free. The same comparison was not made between RADARSAT 1 and Landsat because although coincident images existed in the original set of 72 RADARSAT 1 images, initial tests revealed these were scenes that had significant issues related to wind and ice and were therefore among the 51 RADARSAT 1 scenes eliminated from the final set. Visual comparisons between QuickBird imagery and Landsat and RADARSAT open water and flooded vegetation show good correspondence between all three (Figure 4). Open water and flooded vegetation maps were also compared between all coincident RADARSAT 2 and Landsat scenes; an example comparison is shown over a large portion of the floodplain east of Maugerville in Figure 5.

A co-occurrence matrix between corresponding Landsat and 30 m nearest neighbor resampled RADARSAT 2 flood maps is shown in Table 2. This matrix represents the sum of eleven co-occurrence matrices representing each of the eleven RADARSAT 2 scenes with coincident Landsat scenes. Overall agreement between Landsat and RADARSAT 2 flood maps was 97.6% with a kappa of 0.865, representing almost perfect agreement between maps produced from different data. Of the three classes, agreement within the flooded vegetation class was lowest. 436 km<sup>2</sup> was classified as flooded vegetation in RADARSAT 2, 174 km<sup>2</sup> or 40.0% of which was classified as land in Landsat, while of 322 km<sup>2</sup> of flooded vegetation mapped in Landsat maps, 121 km<sup>2</sup> or 37.7% was classified as open water in RADARSAT 2.

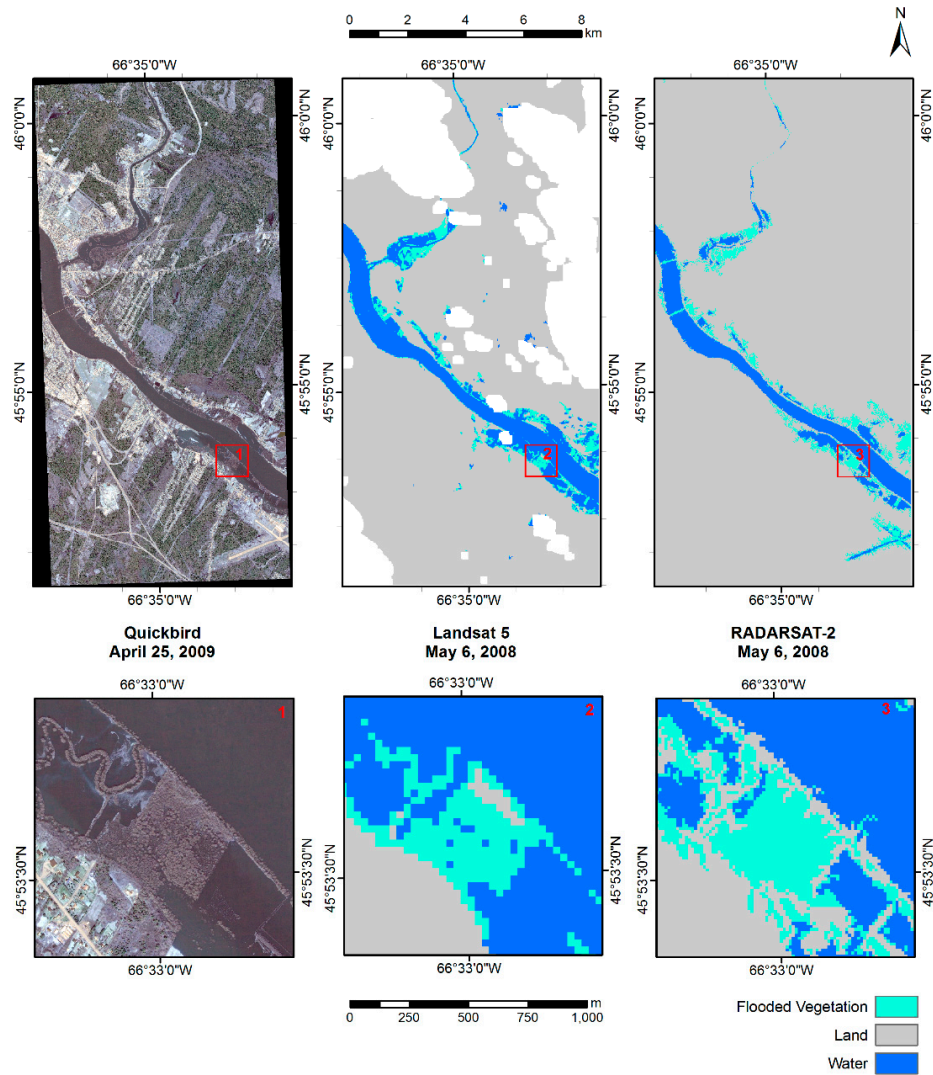


**Figure 4.** Natural color QuickBird image (left) representing similar water levels to Landsat (middle) and RADARSAT 2 (right) open water and flooded vegetation maps, with example insets along the bottom. No-data representing cloud and cloud shadow are white in optical imagery.

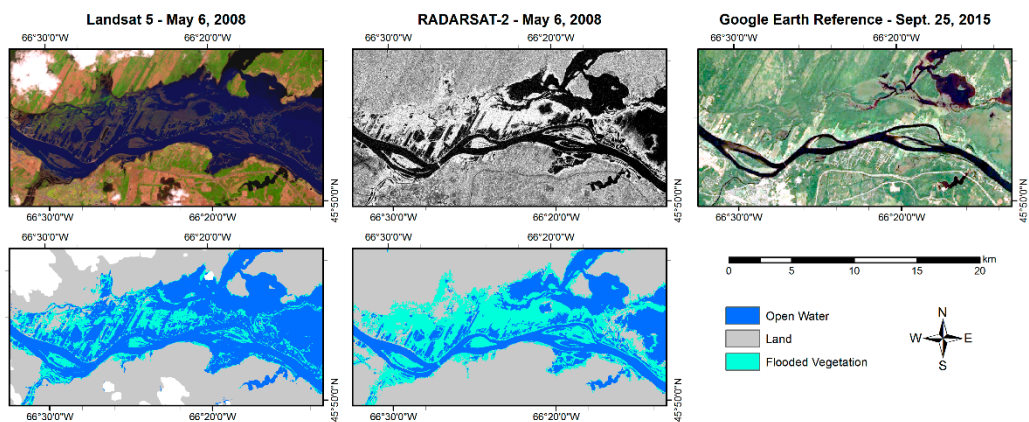


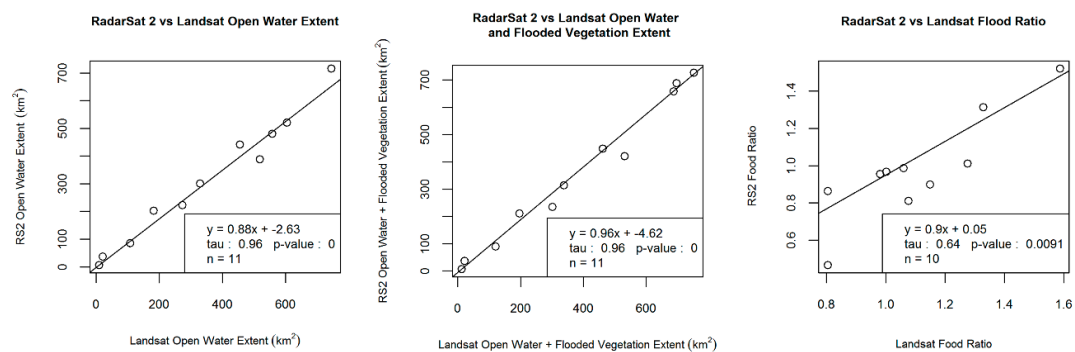
**Figure 5.** Coincident open water and flooded vegetation maps from Landsat and RADARSAT 2 of the main portion of the Saint John River floodplain east of Maugerville. No-data representing cloud and cloud shadow are white in optical imagery.

**Table 2.** Co-occurrence between coincident Landsat and RADARSAT 2 flood maps. Units are in square kilometers.

		Landsat			Sum
		Open Water	Land	Flooded Veg	
RADARSAT 2	Land	3361	177	55	3593
	Open Water	374	38,236	121	38,731
	Flooded Veg	174	116	145	436
	Sum	3909	38,529	322	
				Overall agreement	97.6%
				Kappa	0.865

Table 2 and plots of corresponding flood extents by sensor shown in Figure 6 revealed approximately eight percent less open water area in RADARSAT than in Landsat, while RADARSAT underestimated combined open water and flooded vegetation by 4.7 percent compared to Landsat for this sample of scenes. Tau rank-based correlations [46] between corresponding open water and combined open water and flooded vegetation extents were both significant at  $p$ -value  $< 0.001$ ; however, a direct comparison includes variance in surface water extents due to different areas mapped beneath common clear-sky Landsat and coincident RADARSAT image footprints for each image pair. In order to remove this variance, a flood ratio was calculated (Equation (1)) as the combined open water and flooded vegetation extent divided by the area of NHN permanent water in the same image footprint. The flood ratio represents an inflation factor of flood extent to NHN water, where a value less than one indicates water extents less than baseline NHN extents, and a value greater than one indicates flooding. The flood ratio was calculated for 10 of 11 Landsat scenes due to extreme cloud cover in one scene beneath the matching RADARSAT 2 image footprint. For the remaining 10 Landsat and RADARSAT 2 scenes, the tau correlation between corresponding flood ratios was significant at  $p < 0.01$  (Figure 6).

$$\text{Flood Ratio} = (\text{Open Water} + \text{Flooded Vegetation}) / \text{NHN Permanent Water}_{\text{image}} \quad (1)$$

**Figure 6.** Comparisons of open water (left) and combined open water and flooded vegetation (middle) between temporally and spatially coincident Landsat and RADARSAT maps, and derived flood ratios (right).

### 3.3. Comparisons between Mapped Flood Extents and Hydrometric Water Depth

Average water depth between Maugerville located upstream, and Oak Point located downstream of the main floodplain near Gagetown was related to combined open water and flooded vegetation extent in the study mask covering the region. For both RADARSAT and Landsat, a normalized flood extent [3] was calculated (Equation (2)) to account for different areas imaged among scenes caused by RADARSAT tasking that produces variable image footprints, and cloud cover in Landsat. The normalized flood extent is the product of the flood ratio times the area of NHN permanent water

beneath the study area mask, providing an approximation of flood extent in the entire study including areas missed by each RADARSAT scene, or areas obscured in Landsat by cloud cover. An assumption of the normalized flood extent is that the flood ratio beneath the mapped area is representative of the flood ratio for the whole study area. Both RADARSAT and Landsat flood extents were significantly related to water depth at  $p$ -value < 0.001 (Figure 7).

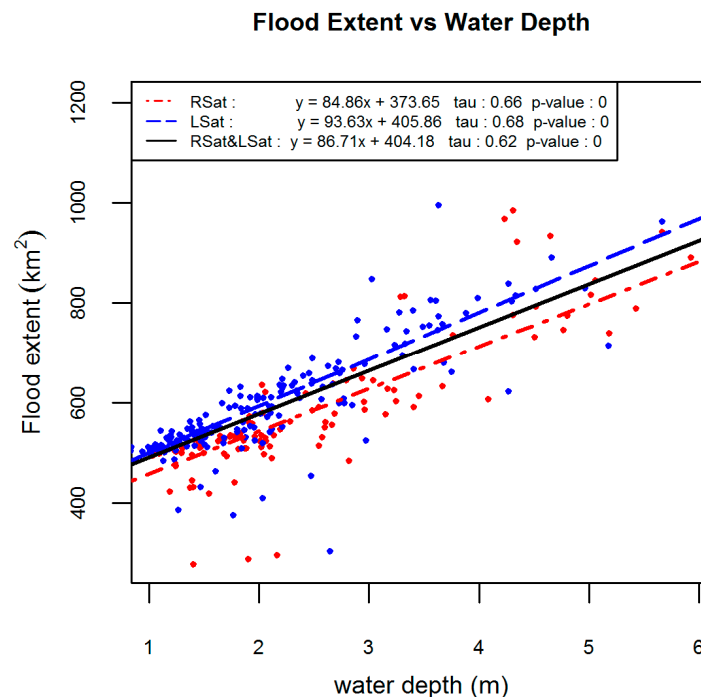


**Figure 7.** Comparisons between normalized flood extents from RADARSAT, Landsat and combined and average daily hydrometric water depth at Maugerville and Oak Point on corresponding satellite acquisition dates.

Analysis of covariance (ANCOVA) was used to determine if the relation between flood extent and flood depth was similar between sensors. Results of ANCOVA revealed that both slope and intercept were similar at  $p < 0.05$  between RADARSAT and Landsat flood depth–extent relations. Therefore, both sensors’ water depths and extents were combined, revealing a combined relation that was also significant at  $p$ -value < 0.001 (Figure 7).

$$\text{Normalized Flood Extent} = \text{Flood Ratio} \times \text{NHN Permanent Water}_{\text{mask}} \quad (2)$$

### 3.4. Inundation Frequencies

A comparison of inundation frequency extents in the study area was made among Landsat and RADARSAT products (Table 3), including Pekel’s global water occurrence product created from 1984–2015 Landsat on Google’s Earth Engine using an expert system classifier (Figure 8) [30]. The Landsat open water and inundation product spanning 1985–2016 contained more total inundated area than Pekel’s 1984–2015 product by nearly 20%. Pekel’s product included no permanent water according to a 100% inundation frequency criterion, but most of the water in the 75% and above category was considered permanent. In this case, Pekel’s product underestimated permanent water by less than 9% compared to our Landsat product using the same permanent water criterion. Combined Landsat open water and flooded vegetation from 1985–2016 contained 12% more flood area than open water alone, most of which is in the least frequent inundation class (1–25%), and second most in the permanent water class (100%).

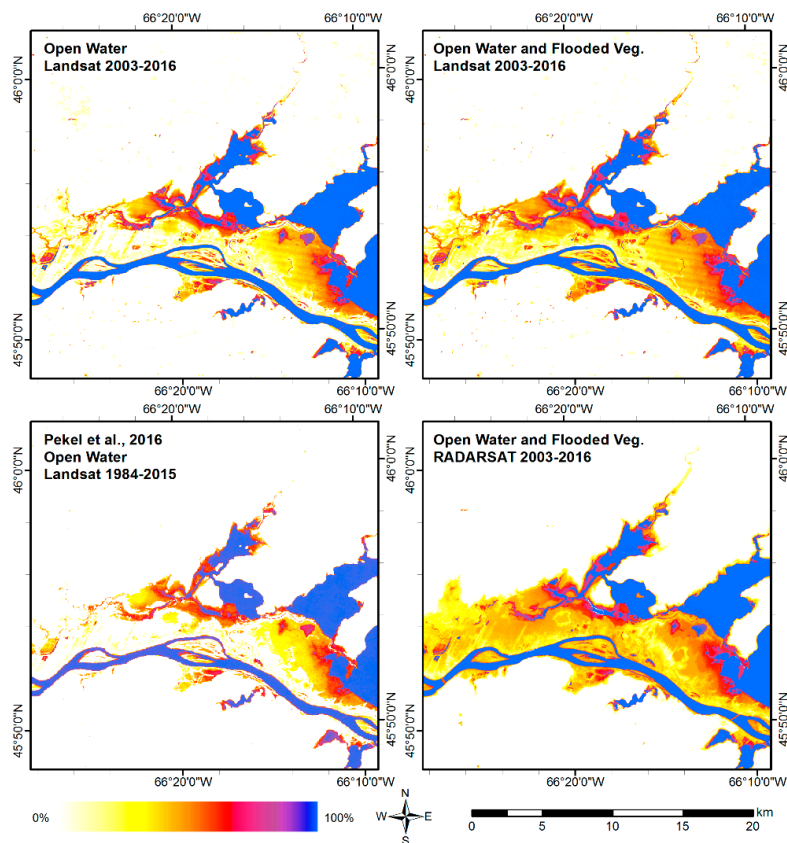


**Figure 8.** Open water (top left) and combined open water and flooded vegetation (top right) inundation frequency from Landsat for the 2003–2016 period, Pekel et al.’s 1984–2015 water occurrence product (bottom left) and 2003–2016 RADARSAT open water and flooded vegetation inundation (bottom right) over the main portion of the Saint John River floodplain east of Maugerville.

**Table 3.** Inundation frequency area by product in the study area mask. OW = Open Water; FV = Flooded Vegetation.

Year 1985–2016				
	Landsat OW	Landsat OW + FV	Pekel [30] 1984–2015	
Inundation frequency range	area (km <sup>2</sup> )			
0	2277	2181	2408	
1–25	163	236	80	
25–50	81	98	79	
50–75	35	38	31	
75–99	262	227	467	
100	246	285	0	
Total inundated area (km <sup>2</sup> )	788	884	657	
Year 2003–2016				
	Landsat OW	Landsat OW + FV	RADARSAT OW	RADARSAT OW + FV
Inundation frequency range	area (km <sup>2</sup> )			
0	2277	2199	2342	2105
1–25	162	208	135	354
25–50	80	97	69	81
50–75	35	44	34	35
75–99	235	206	233	147
100	276	312	260	351
Total inundated area (km <sup>2</sup> )	788	866	730	967

A comparison of Landsat open water inundation frequency products from 1985–2016 and 2003–2016 revealed the same total inundated area for both, with approximately 12% more permanent water in the 2003–2016 product. Combined open water and flooded vegetation also contained more permanent water in the 2003–2016 period, while containing less total inundated area overall.

RADARSAT open water inundation frequency occupied less area than Landsat open water because RADARSAT underestimated single date open water extents by about 8% compared to Landsat. Combined open water and flooded vegetation inundation was greater in RADARSAT compared to Landsat by about 12%, mainly due to infrequently inundated vegetation in the 1–25% class, and permanently inundated vegetation.

### 3.5. Inundation Trends

A comparison between pixel-based Landsat and RADARSAT logistic trend images from 2003–2016 showed that although trend direction and significance were highly related between sensors, few common areas were significant at  $p < 0.05$  in both. The RADARSAT trend image shown in Figure 9 appears less noisy than the Landsat trend image due in large part to striping caused by Scan Line Corrector (SLC) failure of Landsat 7 post 2003, with areas becoming significantly more inundated (wetter) in blue and areas becoming significantly less inundated (drier) in red. The RADARSAT trend image shows increasing inundation frequency around most permanent water bodies, especially along the Saint John River shoreline. The width of the significantly trended shoreline is less than six RADARSAT pixels (75 m) along most of its length. These significant wetting trends only appeared as single pixels along portions of shoreline in Landsat due to its coarser resolution and the effect of mixed pixels. Hydrometric data confirmed that median summer water levels have increased significantly from 1985–2016 at  $p < 0.05$  at an average rate of between 1.0 and 1.5 cm per year at Maugerville and Oak Point stations, while 2003–2016 levels were also positively trended but not significant. Increasing water depth may have led to greater extent on its own since the two measures are significantly related, or may have contributed to shoreline erosion that further increased nearshore inundation except on western, upstream shorelines of islands where deposition appears to have occurred.

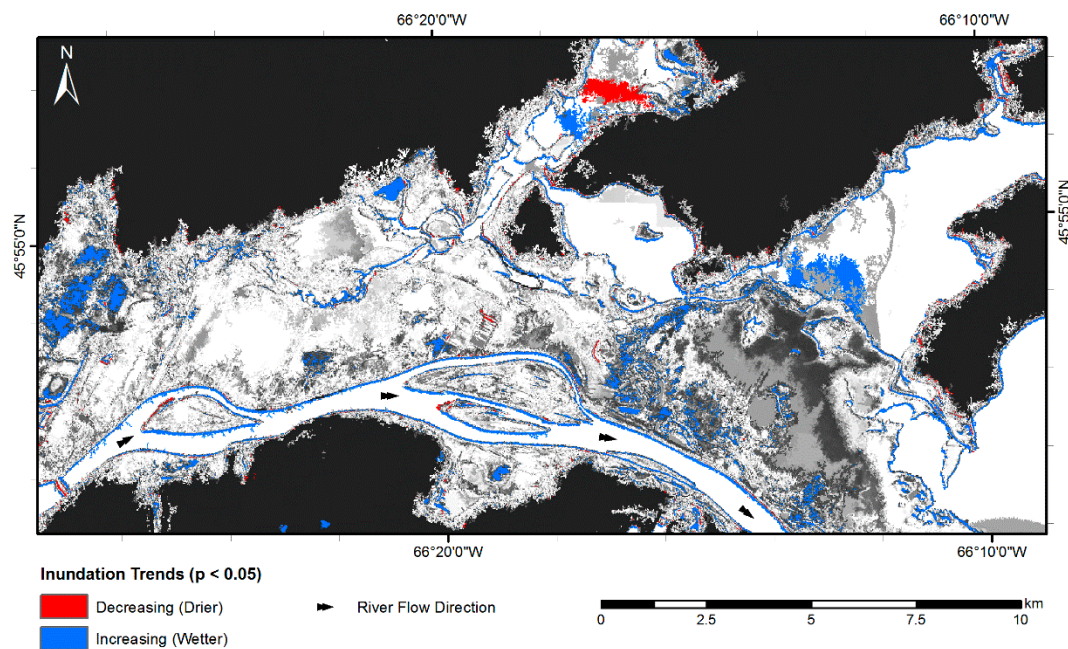


**Figure 9.** 2003–2016 RADARSAT inundation trends with significant decreasing inundation (drying) in red, and significant increasing inundation (wetting) in blue over the main portion of the Saint John River floodplain east of Maugerville.

#### 4. Discussion

Classification simulations showed that open water classification accuracy remained high as long as training labelling errors did not exceed 20%. Training errors in the range of 30–40% negatively impacted random and omission errors by less than 5%, while commission error was less than 5% in the 40–50% labelling error range. This was true whether pixels were randomly labelled as the opposite land/water class (random error), water pixels were randomly assigned to land (water omission), or land pixels were randomly assigned to water (water commission). This suggests that See 5 decision trees are highly robust to training data labelling error, as differences between RADARSAT and permanent land and water from historical inundation can be up to 30–40% without incurring a significant penalty in classification accuracy. By simulating symmetric noise in a two-class classification problem, [38] also determined that decision tree accuracies were nearly as good at 30% noise as at 0% noise provided a sufficiently large training sample ( $N > 10000$ ). The classification problem presented in this paper easily meets this sample size criterion, leading to similar results and conclusions.

Comparisons between open water and flooded vegetation maps from Landsat and RADARSAT acquired on the same dates showed that using the current classification methodologies, RADARSAT underestimated open water extents compared to Landsat, but the combined area of open water and flooded vegetation was only slightly higher for Landsat. These discrepancies relate to differences in the amount of vegetation detectable by each sensor. In leaf-off conditions, sensing water through a vegetated canopy near nadir will obscure branches and trunks due to low contrast between dark features including tree bark, shadow and water [13–15]. At oblique angles and low levels of vegetation cover however, radar still produces double bounce off of trunks and standing water acting as corner reflectors. Therefore, radar appears generally more sensitive to lower flooded vegetation biomass levels than optical. The fact that radar overestimates flooded vegetation compared to optical also accounts for the fact that radar relatively underestimates open water. Forty percent of the area mapped as flooded vegetation in RADARSAT was classified as open water in corresponding Landsat, confirming a greater sensitivity of RADARSAT to low flooded vegetation biomass levels. Therefore, the vegetation biomass threshold value between open water and flooded vegetation is higher in optical than in radar, while both detect a similar amount of overall flooding.

Both sensors' total flood extent showed similarly significant rank-based correlations with coincident hydrometric water depth. Daily hydrometric water depth represents a daily mean while flood extents represent conditions at the time of the satellite overpass. Discrepancies between the two relative measures of flood severity can occur due to changes in river bathymetry between years, as well as the dynamic nature of flooding caused by flow obstructions and surges from snowmelt and precipitation. A strong dependence of flood extent on water depth suggests a monotonic relation over the duration of the time-series, which would indicate that other factors that interact with depth to produce flood extent such as bathymetry and obstructions have had relatively little effect on the relationship through time. Therefore, flood extents can be predicted from flood depth from year to year with some uncertainty, suggesting that similar impacts of previous events can be expected in subsequent years dependent on water depth.

Inundation products reflect differences due to input data. More detailed inundation frequency and visually cleaner inundation trends were observed in RADARSAT than in Landsat. This may be caused by the effects of RADARSAT's finer spatial resolution in standard and wide-beam modes and residual atmospheric contamination in Landsat after the application of FMask. The number of valid per-pixel observations in the Landsat image stack is dependent on cloud and cloud shadow, while in RADARSAT the number of observations is due to overlap among image footprints that vary between dates. The mean number of valid observations within the study area in the 2003–2016 Landsat image stack containing 114 images was slightly less than 70, or 61%. In RADARSAT, the average number of valid observations in the study area was 77 of 131 dates of imagery, or 59%. The percentage of valid observations depends on several factors, including regional cloud cover and RADARSAT tasking, which is determined by the occurrence of flood events and the need for flood information. It is

expected that in many floodplains in Canada that experience seasonal flooding and where cloud cover is similar to New Brunswick, the number of valid observations used to calculate inundation frequency and trends should be similar between Landsat and RADARSAT.

Total inundation including open water and flooded vegetation was greater in RADARSAT than in Landsat. Mean hydrometric water depth was approximately 45 cm greater on RADARSAT acquisition dates than on Landsat dates and maximum water depth was 29 cm greater (Table 1) due to the fact that a relatively high percentage of RADARSAT scenes were tasked during flood events. Coincident RADARSAT 2 and Landsat flood extents showed that both open water and combined open water and flooded vegetation was greater in Landsat, but that flooded vegetation area was greater on its own in RADARSAT 2. Despite greater combined open water and flooded vegetation extents in Landsat scenes, a larger combined open water and flooded vegetation inundation area in RADARSAT was likely due in part to greater hydrometric water depth during flood events imaged by RADARSAT.

Pekel's occurrence product [30] predicted the least inundation area compared to our Landsat or RADARSAT products, regardless of the period analyzed. While this result suggests greater than 5% global omission reported in [30], the area analyzed here represents a small subset of a global product. Therefore, either the St-John region is not representative of global water omission or perhaps more likely, their underestimation of inundation area is due to the size of their mapping endeavor and the need for robust, conservative methods to ensure good performance across a range of conditions. Despite missing some inundation including flooded vegetation, Pekel's product omits less than 20% inundation compared to ours, which will translate into a small mapping error if this product were used to train a classifier to predict open water with the current methodology. A classifier was trained by sampling scene-specific land and water signatures beneath Pekel's occurrence map to predict open water extent over the same RADARSAT scene used for error analysis, producing a slightly lower kappa of 0.82 when evaluated against NHN water extents, compared to 0.84 for our product. During the 2017 flood activation for Eastern Ontario and Western Quebec including cities of Ottawa/Gatineau and Montreal, the Emergency Geomatics Services at Natural Resources Canada used Pekel et al.'s occurrence product in the current methodology to generate near real-time flood maps from a range of sensors. Pekel's occurrence and the method were tested successfully on data received through the International Space Charter for Disasters from Sentinel-1, TerraSar-X, ALOS-2 and KOMPSAT 5 in addition to RadarSat-2 [47].

Inundation frequency is a product that is useful on its own to inform public safety, land use and insurance, among others, on historical surface water patterns. Historical inundation is also useful to generate land and water masks to train machine learning and produce current surface water maps, as was done in near real-time during EGS's 2017 flood activation. Going forward, the approach of generating real-time and historical water maps will be an iterative one, in which current flood products are used to update and improve historical inundation products, which will in turn be used to produce flood products next season. This feedback will continue to improve mapped water extents in near real-time and historically.

## 5. Conclusions

Inundation frequency has routinely been mapped from historical Landsat data, but not from RADARSAT imagery until now. Landsat has been the default sensor for these types of analyses due to its data availability, consistency and long record. Currently, the RADARSAT image archive is only available free of charge to the Government of Canada, which has limited its use for historical analyses. However, RADARSAT appears to offer some advantages over Landsat for dynamic surface water mapping. First, it has the known advantage of cloud penetration while performing well for open water detection under the right weather conditions. This allows radar to detect and map peak flood extents regardless of weather, enabling mapping of the full extent of periodic inundation that is critical to land use decisions. Second, though not confirmed by field data, it appears to be sensitive to less flooded vegetation biomass and/or cover than optical, while combined open water and flooded vegetation

extents were similar between sensors. Third, while neither sensor provides a greater number of valid temporal observations than the other for the Saint John River study area, RADARSAT provides more detail in standard and wide coverage modes than Landsat and visibly cleaner inundation frequency and trend images. Given these advantages, it is hoped that the RADARSAT archive is made publicly available to foster development across a broader range of historical time-series applications.

The surface water mapping methodology first developed in [3] and enhanced in the current paper to include flooded vegetation is shown to be robust to sensor type and training error. Knowledge and information embedded in existing surface water maps can be used to train machine learning to predict surface water extents in near real-time. Use of Pekel et al.'s inundation maps and machine learning applied to a range of radar and optical sensors from the Disaster Charter during the 2017 flood activation in Eastern Canada demonstrated the usefulness and efficiency of this approach. New water maps are to be used to update historical inundation maps for mapping future flood events and to provide up to date information to guide future land use decisions.

**Author Contributions:** I.O. designed and conducted the research. S.T.-L. acquired data, provided technical feedback and edited the manuscript.

**Acknowledgments:** The authors acknowledge Thomas Rainville for preparing maps and figures and Robert Fraser for feedback on the paper and internal review.

**Conflicts of Interest:** The authors declare no conflict of interest.

## References

1. Intergovernmental Panel on Climate Change. *Climate Change 2013—The Physical Science Basis: Working Group I Contribution to the Fifth Assessment Report of the Intergovernmental Panel on Climate Change*; Intergovernmental Panel on Climate Change, Ed.; Cambridge University Press: Cambridge, UK, 2014; ISBN 978-1-107-41532-4.
2. Thomas, R.F.; Kingsford, R.T.; Lu, Y.; Hunter, S.J. Landsat mapping of annual inundation (1979–2006) of the Macquarie Marshes in semi-arid Australia. *Int. J. Remote Sens.* **2011**, *32*, 4545–4569. [[CrossRef](#)]
3. Olthof, I. Mapping Seasonal Inundation Frequency (1985–2016) along the St-John River, New Brunswick, Canada using the Landsat Archive. *Remote Sens.* **2017**, *9*, 143. [[CrossRef](#)]
4. Mueller, N.; Lewis, A.; Roberts, D.; Ring, S.; Melrose, R.; Sixsmith, J.; Lymburner, L.; McIntyre, A.; Tan, P.; Curnow, S.; et al. Water observations from space: Mapping surface water from 25 years of Landsat imagery across Australia. *Remote Sens. Environ.* **2016**, *174*, 341–352. [[CrossRef](#)]
5. Verpoorter, C.; Kutser, T.; Seekell, D.A.; Tranvik, L.J. A global inventory of lakes based on high-resolution satellite imagery. *Geophys. Res. Lett.* **2014**, *41*, 2014GL060641. [[CrossRef](#)]
6. Feng, M.; Sexton, J.O.; Channan, S.; Townshend, J.R. A global, high-resolution (30-m) inland water body dataset for 2000: First results of a topographic–spectral classification algorithm. *Int. J. Digit. Earth* **2016**, *9*, 113–133. [[CrossRef](#)]
7. Yamazaki, D.; Trigg, M.A.; Ikeshima, D. Development of a global ~90 m water body map using multi-temporal Landsat images. *Remote Sens. Environ.* **2015**, *171*, 337–351. [[CrossRef](#)]
8. Prigent, C.; Papa, F.; Aires, F.; Jimenez, C.; Rossow, W.B.; Matthews, E. Changes in land surface water dynamics since the 1990s and relation to population pressure. *Geophys. Res. Lett.* **2012**, *39*, L08403. [[CrossRef](#)]
9. Brisco, B.; Short, N.; van der Sanden, J.; Landry, R.; Raymond, D. A semi-automated tool for surface water mapping with Radarsat-1. *Can. J. Remote Sens.* **2009**, *35*, 336–344.
10. Wang, Y.; Colby, J.D.; Mulcahy, K.A. An efficient method for mapping flood extent in a coastal floodplain using Landsat TM and DEM data. *Int. J. Remote Sens.* **2002**, *23*, 3681–3696. [[CrossRef](#)]
11. Martinis, S.; Rieke, C. Backscatter Analysis Using Multi-Temporal and Multi-Frequency SAR Data in the Context of Flood Mapping at River Saale, Germany. *Remote Sens.* **2015**, *7*, 7732–7752. [[CrossRef](#)]
12. Yu, Y.; Saatchi, S. Sensitivity of L-Band SAR Backscatter to Aboveground Biomass of Global Forests. *Remote Sens.* **2016**, *8*, 522. [[CrossRef](#)]
13. Mackey, H.E., Jr.; Riley, R.S. Mapping of flood patterns in a 10,000-acre southeastern river swamp with SPOT HRV data. In *ASPRS/ACSM Annual Convention and Exposition*; Technical Paper 1; ASPRS: Reno, Nevada, 1994; p. 375.

14. Townsend, P.A.; Walsh, S.J. Modeling floodplain inundation using an integrated GIS with radar and optical remote sensing. *Gemorphology* **1998**, *21*, 295–312. [[CrossRef](#)]
15. Lang, M.; McCarty, G.; Oesterling, R.; Yeo, I.-Y. Topographic Metrics for Improved Mapping of Forested Wetlands. *Wetlands* **2013**, *33*, 141–155. [[CrossRef](#)]
16. Roy, D.P.; Zhang, H.K.; Ju, J.; Gomez-Dans, J.L.; Lewis, P.E.; Schaaf, C.B.; Sun, Q.; Li, J.; Huang, H.; Kovalsky, V. A general method to normalize Landsat reflectance data to nadir BRDF adjusted reflectance. *Remote Sens. Environ.* **2016**, *176*, 255–271. [[CrossRef](#)]
17. White, L.; Brisco, B.; Daboor, M.; Schmitt, A.; Pratt, A. A Collection of SAR Methodologies for Monitoring Wetlands. *Remote Sens.* **2015**, *7*, 7615–7645. [[CrossRef](#)]
18. Freeman, A.; Durden, S.L. A three-component scattering model for polarimetric SAR data. *IEEE Trans. Geosci. Remote Sens.* **1998**, *36*, 963–973. [[CrossRef](#)]
19. Hess, L.L.; Melack, J.M.; Simonett, D.S. Radar detection of flooding beneath the forest canopy: A review. *Int. J. Remote Sens.* **1990**, *11*, 1313–1325. [[CrossRef](#)]
20. Lang, M.; Townsend, P.; Kasischke, E. Influence of incidence angle on detecting flooded forests using C-HH synthetic aperture radar data. *Remote Sens. Environ.* **2008**, *112*, 3898–3907.
21. Bolanos, S.; Stiff, D.; Brisco, B.; Pietroniro, A. Operational surface water detection and monitoring using RADARSAT 2. *Remote Sens.* **2016**, *8*, 285. [[CrossRef](#)]
22. O'Grady, D.; Leblanc, M.; Gillieson, D. Relationship of local incidence angle with satellite radar backscatter for different surface conditions. *Int. J. Appl. Earth Obs. Geoinf.* **2013**, *24*, 42–53.
23. Li, J.; Wang, S. An automatic method for mapping inland surface waterbodies with RADARSAT-2 imagery. *Int. J. Remote Sens.* **2015**, *36*, 1367–1384. [[CrossRef](#)]
24. Woodhouse, I.H. *Introduction to Microwave Remote Sensing*; CRC Press: Boca Raton, FL, USA, 2005.
25. Henry, J.-B.; Chastanet, P.; Fellah, K.; Desnos, Y.-L. Envisat multi-polarized ASAR data for flood mapping. *Int. J. Remote Sens.* **2006**, *27*, 1921–1929. [[CrossRef](#)]
26. White, L.; Brisco, B.; Pregitzer, M.; Tedford, B.; Boychuk, L. RADARSAT-2 Beam Mode Selection for Surface Water and Flooded Vegetation Mapping. *Can. J. Remote Sens.* **2014**, *40*, 135–151. [[CrossRef](#)]
27. Schowengerdt, R.A. *Remote Sensing, Third Edition: Models and Methods for Image Processing*, 3rd ed.; Academic Press: Burlington, MA, USA, 2006; ISBN 978-0-12-369407-2.
28. Pax-Lenney, M.; Woodcock, C.E.; Macomber, S.A.; Gopal, S.; Song, C. Forest mapping with a generalized classifier and Landsat TM data. *Remote Sens. Environ.* **2001**, *77*, 241–250. [[CrossRef](#)]
29. Song, C.; Woodcock, C.E. Monitoring forest succession with multitemporal Landsat images: Factors of uncertainty. *IEEE Trans. Geosci. Remote Sens.* **2003**, *41*, 2557–2567. [[CrossRef](#)]
30. Pekel, J.-F.; Cottam, A.; Gorelick, N.; Belward, A.S. High-resolution mapping of global surface water and its long-term changes. *Nature* **2016**, *540*, 418–422. [[CrossRef](#)] [[PubMed](#)]
31. Kuenzer, C.; Guo, H.; Huth, J.; Leinenkugel, P.; Li, X.; Dech, S. Flood Mapping and Flood Dynamics of the Mekong Delta: ENVISAT-ASAR-WSM Based Time Series Analyses. *Remote Sens.* **2013**, *5*, 687–715. [[CrossRef](#)]
32. Zhu, Z.; Wang, S.; Woodcock, C.E. Improvement and expansion of the Fmask algorithm: Cloud, cloud shadow, and snow detection for Landsats 4–7, 8, and Sentinel 2 images. *Remote Sens. Environ.* **2015**, *159*, 269–277. [[CrossRef](#)]
33. Chander, G.; Markham, B.L.; Helder, D.L. Summary of current radiometric calibration coefficients for Landsat MSS, TM, ETM+, and EO-1 ALI sensors. *Remote Sens. Environ.* **2009**, *113*, 893–903. [[CrossRef](#)]
34. Quinlan, J.R. *C4.5: Programs for Machine Learning*; Morgan Kaufmann Publishers Inc.: San Francisco, CA, USA, 1993; ISBN 978-1-55860-238-0.
35. Ali, I.; Greifeneder, F.; Stamenkovic, J.; Neumann, M.; Notarnicola, C. Review of Machine Learning Approaches for Biomass and Soil Moisture Retrievals from Remote Sensing Data. *Remote Sens.* **2015**, *7*, 16398–16421. [[CrossRef](#)]
36. Latifovic, R.; Pouliot, D.; Olthof, I. Circa 2010 land cover of Canada: Local optimization methodology and product development. *Remote Sens.* **2017**, *9*, 1098. [[CrossRef](#)]
37. Kasischke, E.S.; Melack, J.M.; Dobson, C. The use of imaging radars for ecological applications—A review. *Remote Sens. Environ.* **1997**, *39*, 141–156. [[CrossRef](#)]
38. Ghosh, A.; Manwani, N.; Sastry, P.S. On the Robustness of Decision Tree Learning under Label Noise. *arXiv*, **2016**, arXiv:1605.06296..
39. Cohen, J. A coefficient of agreement for nominal scales. *Educ. Psychol. Meas.* **1960**, *20*, 37–46. [[CrossRef](#)]

40. Myneni, R.B.; Keeling, C.D.; Tucker, C.J.; Asrar, G.; Nemani, R.R. Increased plant growth in the northern high latitudes from 1981 to 1991. *Nature* **1997**, *386*, 698–702. [[CrossRef](#)]
41. Pouliot, D.; Latifovic, R.; Olthof, I. Trends in vegetation NDVI from 1 km AVHRR data over Canada for the period 1985–2006. *Int. J. Remote Sens.* **2009**, *30*, 149–168. [[CrossRef](#)]
42. Olthof, I.; Fraser, R.H.; Schmitt, C. Landsat-based mapping of thermokarst lake dynamics on the Tuktoyaktuk Coastal Plain, Northwest Territories, Canada since 1985. *Remote Sens. Environ.* **2015**, *168*, 194–204. [[CrossRef](#)]
43. Buermann, W.; Wang, Y.; Dong, J.; Zhou, L.; Zeng, X.; Dickinson, R.E.; Potter, C.S.; Myneni, R.B. Analysis of a multiyear global vegetation leaf area index data set. *J. Geophys. Res.* **2002**, *107*, 4646. [[CrossRef](#)]
44. Pradhan, B. Flood susceptible mapping and risk area delineation using logistic regression, GIS and remote sensing. *J. Spat. Hydrol.* **2010**, *9*, 1–18.
45. Lee, S. Application of logistic regression model and its validation for landslide susceptibility mapping using GIS and remote sensing data. *Int. J. Remote Sens.* **2005**, *26*, 1477–1491. [[CrossRef](#)]
46. Kendall, M.G.; Stuart, A. Influence and Relationship. In *The Advanced Theory of Statistics*; Griffin: London, UK, 1967; Volume 2.
47. Olthof, I.; Tolszczuk-Leclerc, S.; Lehrbass, B.; Shelat, Y.; Neufeld, V.; Decker, V. *New Flood Mapping Methods Implemented during the 2017 Spring Flood Activation in Southern Quebec*; Open File 38; Natural Resources Canada: Ottawa, ON, Canada, 2018.



© 2018 by the authors. Licensee MDPI, Basel, Switzerland. This article is an open access article distributed under the terms and conditions of the Creative Commons Attribution (CC BY) license (<http://creativecommons.org/licenses/by/4.0/>).